Towards single-scan quantum state tomography of photoelectrons

Master's thesis

Samuel Eklund

Supervisor: David Busto
Assistant supervisor: Anne L'Huillier
Examiner: Lars Rippe

LUNDS UNIVERSITET

LRAP: 600
Division of Atomic Physics
Department of Physics
Faculty of Engineering
Lund University, Sweden
June 2024

Contents

Abstract

Today's gold standard for measuring the quantum state of a given quantum mechanical system is quantum state tomography. By preparing many identical states and performing projective measurements on them, their quantum state, described by the density matrix, can be reconstructed. A protocol called Kvanttillstånds-tomogRafi av AttoseKund-ElektroNvågpaket (KRAKEN) has been developed to perform quantum state tomography on photoelectrons. The protocol characterises the quantum state photoelectron wave packets created by ionisation of atoms by XUV pulses using photoelectron interference induced by a bichromatic IR field. In this project, a modified version of KRAKEN called poly-KRAKEN is implemented experimentally. By extending the probe field to include more spectral components, a larger part of the density matrix is obtained in a single measurement. The poly-KRAKEN protocol is used to reconstruct the density matrix of photoelectrons emitted from argon atoms. The obtained density matrix shows an elliptical pattern, indicating a partially coherent state.

Vi kan mäta egenskaper hos fotoelektroner!

När ljus med tillräckligt hög energi träffar ett material kan en elektron frigöras från materialet. Detta beskrevs av Einstein i början av 1900-talet som den fotoelektriska effekten. Genom att mäta rörelseenergin hos de frigjorda elektronerna, eller fotoelektronerna, kan man avgöra egenskaper hos olika material.

Dessa mätmetoder baseras på att fotoelektronen är en partikel, men den är också ett kvantobjekt. Ett sådant kvantobjekt beskrivs med kvantfysik, den teori som beskriver system på mycket liten skala, så som atomer och molekyler. Egenskaperna hos ett kvantobjekt beskrivs av ett så kallat kvanttillstånd.

Ett fenomen inom kvantfysik, som det inte finns någon motsvarighet för i den ”vanliga” världen, är sammanflätning. När två kvantobjekt är sammanflätade delar de någon egenskap och man kan, genom att mäta egenskapen på det ena kvantobjektet, direkt veta motsvarande egenskap för det andra kvantobjektet. Då en fotoelektron frigörs i det som beskrevs som den fotoelektriska effekten, där en elektron absorberar en foton och lämnar kvar en jon i materialet, kan fotoelektronen vara sammanflätad med den kvarlämnade jonen. För att fullständigt mäta fotoelektronens kvanttillstånd när den är sammanflätad med den kvarlämnade jonen räcker det inte att enbart mäta rörelseenergin hos fotoelektronen, utan en annan mätmetod krävs.

I Lund har en metod för att göra sådana mätningar utvecklats. Genom att förbereda många identiska fotoelektroner, och mäta dessa, kan man successivt återskapa kvanttillståndet av fotoelektronen. En begränsning med denna metod är att enbart en liten del av kvanttillståndet kan mätas i taget. Därför måste många mätningar göras, vilket i sin tur tar mycket lång tid. I detta projekt har jag implementerat en metod som låter oss mäta en större del av kvanttillståndet i en enda mätning. Framgent kan denna metod användas för att studera sammanflätningsprocesser i olika typer av material samt för att ta reda på egenskaper hos den kvarlämnade jonen.

Acknowledgement

Firstly, I would like to thank my supervisors David and Anne. Thank you David for always supporting and guiding me throughout the various parts of this project and thesis. Whether discussing theory or experiments, you always took the time to answer all of my questions and to explain everything thoroughly. You made the work of this master's thesis a great experience. Thank you Anne for your valuable comments and for showing such enthusiasm for the experimental results.

I would also like to thank Gustav and Hugo, the office of A305, for all the hours we spent together in both the office and the lab. Thank you Gustav for a good collaboration during this project, and also, for all the labs and projects we have worked on together throughout our time at university. Thank you Hugo for the late evening discussions about atomic physics and all the lunches at the nation.

I would like to thank the members of the attolab. Thank you Mattias for always bringing a positive energy and for explaining every small detail of the lab with eager. Thank you Edoardo for all the hours we spent together in the lab, and for the ducks. Thank you Robin for showing me how to produce good looking figures in MATLAB and for, at multiple occasions, coming in to the lab at midnight just to turn off the laser after a three or four hour scan. Thank you Christoph for providing a more theoretical aspect to this project.

Thank you to the rest of the attogroup as well as the Division of Atomic Physics. It has been a pleasure to spend the time of my master's thesis here!

Lastly, I would like to thank my family and friends for the immense support, not only throughout the duration of this project but also during my time at university.

Chapter 1

Introduction

1.1 Background

The photoelectric effect was first observed by Hertz in the late 1800s [1] and then described by Einstein in the early 1900s [2]. It was discovered that when materials are exposed to light, it can result in the emission of electrons from the material. This effect was only observed for light up to a certain wavelength, independent of the intensity of the light. To explain this phenomenon, Einstein introduced a quantum of energy, that is transferred from the light to the electrons in the material. This quantum of energy, $E = \hbar\omega$, with $\hbar$ the reduced Planck constant and ω the angular frequency of the light, gave rise to the concept of the photon.

Since the description of the photoelectric effect, the technique of photoelectron spectroscopy has been developed to study the properties of matter. In order for a photoelectron to be emitted due to an incident photon, its energy needs to be higher than the ionisation potential of the atom, $\hbar\omega > I_p$, where I_p is the ionisation potential of the atom. The resulting photoelectron has a kinetic energy of $E_{kin} = \hbar\omega - I_p$. By measuring the photoelectrons emitted in the process of photoionisation, information of the properties of the material can be obtained. This led to the possibility to study the electronic structure of atoms, and to characterise different materials. Considering the quantum nature of the photoelectron, it can also be described by a wave packet. Standard photoelectron spectroscopy described above, only give access to the amplitude of the wave packet.

The discovery of high harmonic generation in the 1980s [3] and the first observation of an attosecond pulse trains in the early 2000s [4] has opened up the possibility to not only study the amplitude of the photoionisation process, but also to gain information about the spectral phase of the wavepacket, providing information on the temporal dynamics

of the photoionisation process [5, 6]. By ionising atoms with short pulses and study the interference of the resulting electron wave packets, both the amplitude and the phase of the photoelectron can be determined.

If the photoelectron is not in a pure state, the quantum state can not be described by a wave function. This calls for the more general formulation of the density matrix to describe the quantum state. Recently, two protocols for determining the density matrix of photoelectrons have been developed. They are based on quantum state tomography, where many identical photoelectron states are prepared and measured via projective measurements. The two protocols are Mixed-FROG (Frequency Resolved Optical Gating) [7] and KRAKEN (Kvanttillstånds tomogRafi av AttoseKund ElektroNvågpaket) [8]. Mixed-FROG is based on interfering electron wave packets using multi-photon transitions and use an algorithm to reconstruct the density matrix of the photoelectron. KRAKEN is instead based on interfering electron wave packets from two-photon transitions and perform multiple scans to gradually reconstruct the density matrix. In this project a modified version of KRAKEN is implemented to reconstruct the density matrix faster.

1.2 Objective

The goal of this project is to experimentally implement a method for measuring the quantum state of photoelectrons in a single scan. At the Division of Atomic Physics in Lund, the measurement scheme KRAKEN has been developed to measure the before mentioned quantum state. However, the KRAKEN scheme relies on taking multiple measurements, while varying the frequency of a probing component, in order to reconstruct the density matrix describing the quantum state. This project will focus on a modified version of KRAKEN, called poly-KRAKEN. Poly-KRAKEN utilises multiple frequencies of the probing IR-field at once, arranged such that it allows for collection of multiple data points simultaneously and therefore to reconstruct a larger part of the density matrix in a single scan.

1.3 Outline

First, some theory is introduced. The process of high-order harmonic generation, photoionisation and photoelectron interferometry is explained and put in to context with different interferometric techniques. Then, a brief introduction to the idea behind the poly-KRAKEN protocol follows. Following up on the theory part, the experimental setup is introduced. The different modifications to the setup are explained as well as how the experiments were prepared and carried out. Next, the experimental results are presented together with the analysis, leading up to the final result of reduced density matrix am-

plitude. Finally the project is concluded, some potential improvements are discussed and some future work is presented.

Chapter 2

Theory

In this chapter the most important theory related to the KRAKEN experiments is introduced. The photoelectrons that are studied in this project are generated by absorption of a short extreme ultraviolet (XUV) pulse. Therefore, the process of high order harmonic generation (HHG), which is used to generate ultrashort XUV pulses is introduced. Density matrix formalism, applied to photoionization is presented, and also the main theory behind the KRAKEN protocol. Additionally, the idea behind the new poly-KRAKEN protocol is introduced.

2.1 High Harmonic Generation

2.1.1 Attosecond pulses

When ultrashort, high energy laser pulses are focused down into a medium, the electric field can be strong enough to distort the atomic potential, leading to highly non-linear effects. In particular, these non-linear effects can result in the emission of odd high order harmonics of the driving laser field. The amplitude of the harmonics start by decreasing exponentially with increasing order (perturbative region), see Fig. 2.1. Past a certain harmonic order, a plateau region appears where the amplitude of the different harmonics remains almost constant. At even higher harmonics the amplitude starts decreasing exponentially again (cut-off region). [3] The harmonics of the plateau region are phase locked and add up to create an attosecond pulse train. [4]

2.1.2 Three-step model

The generation of high order harmonics can be described by a semi-classical model called the three step model, as developed in [9]. This model illustrates how an electron is ejected

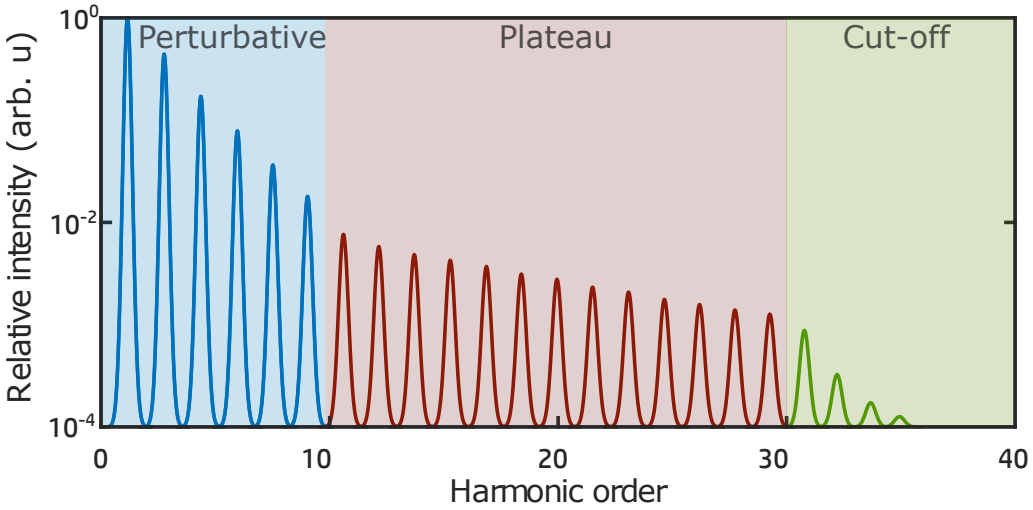

Figure 2.1: An illustration of the harmonic spectrum from high harmonic generation (HHG) showing the perturbative, plateau and cut-off regions.

from an atom by tunnelling out of the atomic potential when the atomic potential is distorted by a strong laser field, builds up energy in the continuum due to the acceleration by the laser field, and then returns to the atom to recombine and emit a high energy photon with energy $E_{photon} = I_p + E_{kin}$. Here I_p is the ionisation potential of the atom and E_{kin} is the kinetic energy of the electron at the time of recombination. Below follows a more detailed description of each of the steps and an overview of the process is shown in Fig. 2.2.

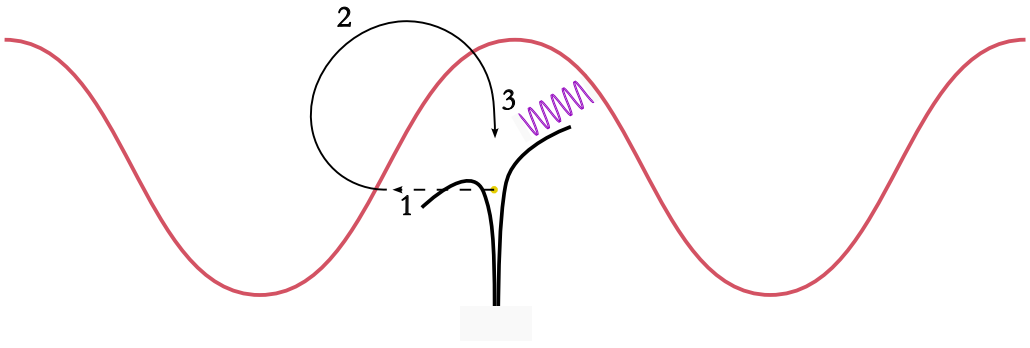

Figure 2.2: Illustration of the three step model showing how (1) the electron tunnels out of the distorted atomic potential, (2) is accelerated in the presence of an electric field and (3) recombines with the ion to emit a high energy photon. The red curve illustrates the driving laser field.

In the first step, as shown in Fig. 2.2, the atomic potential is distorted by the strong laser field, creating a barrier. Around the peak of the laser field the barrier is thin enough so that an electron may tunnel ionise out through the potential, see step 1 in the figure.

In the second step, denoted 2 in Fig. 2.2, the emitted electron travels in the presence of the electric field of the laser. Due to the electric field, the electron is accelerated, resulting in an increase in kinetic energy. The acceleration can be described by the Lorentz force, where the electron is a charged particle propagating in an electric field. Assuming the electric field is classical, it can be described as a sinusoid $E(t) = E_0 \sin(\omega t)$, where E_0 is the peak amplitude of the electric field, ω is the frequency of the electric field and t is time. Now, by solving the classical equation of motion in one dimension, the electron's displacement from the parent ion as a function of time is described by:

$$x(t, t_i) = \frac{eE_0}{m_e\omega^2} \left[\sin(\omega t) - \sin(\omega t_i) - \omega(t - t_i)\cos(\omega t_i)\right], \tag{2.1}$$

where e is the charge of the electron, m_e is the electron mass, ω is the frequency of the driving field and t_i is the time of ionisation. Here it is assumed that the ion is placed at $x = 0$ and that the atom is ionised at $x(t_i) = 0$.

In the third step the electron returns to the atom, where it may recombine. If it recombines, a photon is emitted with energy corresponding to the return energy of the electron plus the ionisation energy of the atom. The return time t_r of the electron can be computed numerically by solving Eq. (2.1) for $x = 0$. Finally, the return kinetic energy is computed by:

$$E_{kin}(t_i, t_r) = 2U_p \left[\cos(\omega t_r) - \cos(\omega t_i)\right]^2, \tag{2.2}$$

where U_p is the ponderomotive energy $U_p = \frac{e^2 E_0^2}{4m_e\omega^2}$. The maximum possible kinetic energy an electron may have when it recombines with its parent ion is approximately $3.17U_p$.

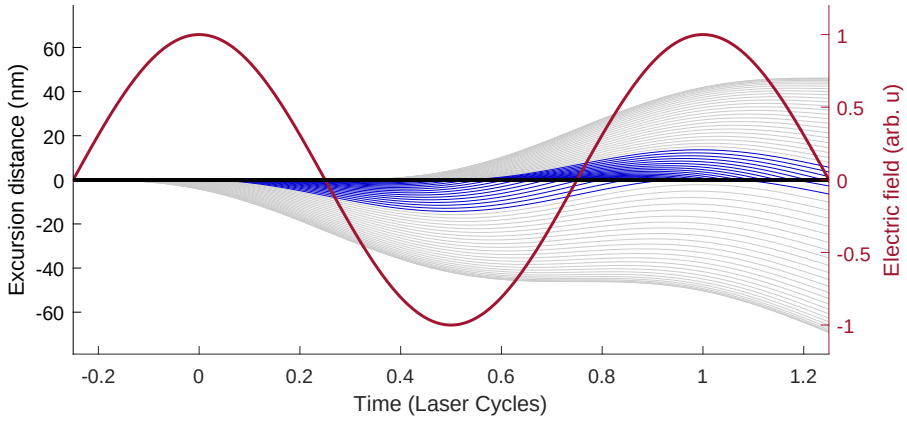

Figure 2.3: An illustration of the electron trajectories as described by the three step model plotted as a function of time. The red curve illustrates the driving laser field, the blue curves are the trajectories of the electrons that return to the ion and the grey curves are the trajectories where the electron escapes the atom and do not recombine. The process is repeated every half laser cycle.

Depending on the time at which the electron tunnels out of the atom, it spends different amount of time in the electric field to build up energy. This results in different electron trajectories. In Fig. 2.3 trajectories with different ionisation times are plotted as a function of time together with the laser field with frequency ω.

2.2 Photoionisation

Now we continue by considering the interaction of XUV light with atoms. When a bound electron in an atom absorbs an incident photon with energy $\hbar\Omega$, which is higher than the ionisation potential I_p of the atom, the electron may be emitted, with kinetic energy

$$E_k = \hbar\Omega - I_p. \tag{2.3}$$

After the ionisation process, the ionic state is $|j\rangle$ and the emitted photoelectron is described by $|\epsilon\rangle$. If the ion+photoelectron system does not interact with the environment, it can be described by the wavefunction [10]:

$$|\Psi_{IE}\rangle = \sum_j \int d\epsilon \; c_j(\epsilon) \, |j\rangle \otimes |\epsilon\rangle \, . \tag{2.4}$$

Now we consider ionisation by monochromatic light in two different atoms, helium and argon. In helium, the ground state is $\left|1s^2\right\rangle$. The resulting state after ionisation is given by

$$|\Psi_{IE}\rangle_{He} = \left|1s^1\right\rangle \otimes |\epsilon\rangle \, . \tag{2.5}$$

In this case, the state is separable, i.e. the individual state of the ion and photoelectron can be described independently.

In argon, the angular momentum $L = 1$ and the spin $S = 1/2$ of the ion couple to each other leading to total angular momenta $J = 1/2$ and $J = 3/2$, such that the ionic ground state splits into two different states: $\left|3p^5 \; P_{3/2}\right\rangle$ and $\left|3p^5 \; P_{1/2}\right\rangle$, with different energies. This phenomenon is called the spin-orbit interaction. Since the energy of the two ionic states is different, depending on the ionic state, the photoelectron will have a different energy due to Eq. (2.3). After ionisation, the state of the ion and photoelectron is:

$$|\Psi_{IE}\rangle_{Ar} = c_{1/2} \left|3p^5 \; {}^2P_{1/2}\right\rangle \otimes |\epsilon_1\rangle + c_{3/2} \left|3p^5 \; {}^2P_{3/2}\right\rangle \otimes |\epsilon_2\rangle \, , \tag{2.6}$$

where $c_{1/2}$ and $c_{3/2}$ are complex coefficients. Equation (2.6) shows that, contrary to helium, the ion and photoelectron are entangled because their individual states cannot be described independently. To describe the quantum state of the individual systems in

a more general form, we now introduce the formulation of the density matrix. To do so, we start by describing the density matrix of the pure bipartite ion+photoelectron state, which is given by:

$$\rho_{IE} = |\Psi_{IE}\rangle \langle\Psi_{IE}| . \tag{2.7}$$

When performing measurements only on the photoelectron, we will not know anything about the ionic states. It is therefore of interest to describe each subsystem independently. Mathematically, this is done using the partial trace operation, defined as [11]:

$$\rho_E = \mathrm{tr_I}(|\Psi_{IE}\rangle \langle\Psi_{IE}|) = \sum_j \langle j| \rho_{IE} |j\rangle . \tag{2.8}$$

In general, the reduced density matrix for the photoelectron is described as

$$\rho_E = \mathrm{tr_I}(|\Psi_{IE}\rangle \langle\Psi_{IE}|) = \iint d\epsilon_1 d\epsilon_2 \sum_j c_j(\epsilon_1) c_j^*(\epsilon_2) |\epsilon_1\rangle \langle\epsilon_2| . \tag{2.9}$$

For helium, when considering ionisation from monochromatic light, and where the photoelectron and ion are not entangled, this results in the following density matrix:

$$\rho_{E_{He}} = |\epsilon\rangle \langle\epsilon| , \tag{2.10}$$

which describes a pure state. However, in argon where spin-orbit splitting (and therefore entanglement) is apparent, the corresponding reduced density matrix is given by

$$\rho_{E_{Ar}} = c_{1/2} |\epsilon_1\rangle \langle\epsilon_1| + c_{3/2} |\epsilon_2\rangle \langle\epsilon_2| , \tag{2.11}$$

which describes a statistical mixture of states.

By now considering light that is not monochromatic, but has a certain spectral width, the photoelectrons can occupy a continuum of states. [8] In this case, the photoelectrons from helium are described by:

$$\rho_{E_{He}}(\epsilon_1, \epsilon_2) = \iint d\epsilon_1 d\epsilon_2 \; c(\epsilon_1) c^*(\epsilon_2) |\epsilon_1\rangle \langle\epsilon_2| , \tag{2.12}$$

whereas in argon, they are described by:

$$\rho_{E_{Ar}}(\epsilon_1, \epsilon_2) = \iint d\epsilon_1 d\epsilon_2 \; \Big(c_{1/2}(\epsilon_1) c_{1/2}^*(\epsilon_2) |\epsilon_1\rangle \langle\epsilon_2| + c_{3/2}(\epsilon_1) c_{3/2}^*(\epsilon_2) |\epsilon_1\rangle \langle\epsilon_2| \Big) . \tag{2.13}$$

2.3 Photoelectron interferometry

In the presence of spatially and temporally overlapping XUV and IR pulses, an atom can undergo two-photon transitions. Consider that an XUV photon generated through HHG is absorbed, taking an electron from the ground state to a continuum state and then that an IR photon is further absorbed or emitted between continuum states. By either absorbing (+) or emitting (-) a photon, the kinetic energy will be shifted up (+) or down (-) by $\hbar\omega$ respectively, giving rise to extra peaks in the photoelectron spectrum. These peaks show up in between every harmonic and are called *sidebands*. [4]

2.3.1 RABBIT

The sideband peaks were first used to characterise the temporal structure of the pulses generated from HHG. For this, the RABBIT technique, short for "Reconstruction of Attosecond Beating By Interference of two-photon Transitions", in [4] was developed. The principle behind RABBIT is illustrated in Fig. 2.4.

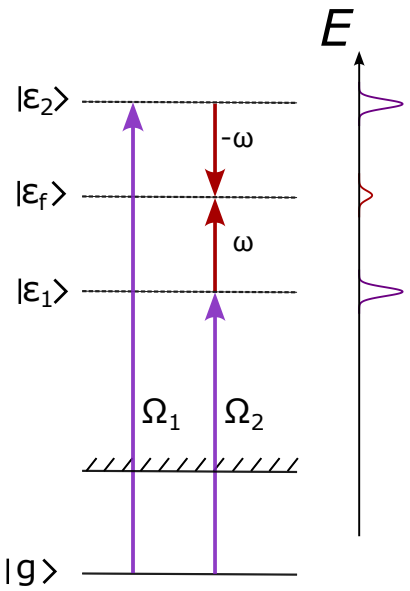

Figure 2.4: Principle of the RABBIT protocol. Two consecutive harmonics ionise the target atom. The emitted photoelectron interacts with the probe IR-field and via two quantum paths ends up in the middle energy, the sideband. On the right is an illustration of the photoelectron spectrum with the two harmonics and the sideband.

Here, $\Omega_1 = (q+1)\omega$ and $\Omega_2 = (q-1)\omega$ are two consecutive harmonics that ionise the atom, creating electron wave packets centered on $|\epsilon_1\rangle$ and $|\epsilon_2\rangle$ respectively. Absorption (emission) of an IR photon from $|\epsilon_1\rangle$ ($|\epsilon_2\rangle$) leads to the same final state $|\epsilon_f\rangle$, resulting in interference of the two ionisation paths. The intensity of the sideband signal using the

RABBIT technique is given by:

$$\begin{aligned} I_q &= \left| M_{q-1}^{(+)} + M_{q+1}^{(-)} \right|^2 \\ &= \left| M_{q-1}^{(+)} \right|^2 + \left| M_{q+1}^{(-)} \right|^2 + 2 \left| M_{q-1}^{(+)} \right| \left| M_{q+1}^{(-)} \right| \cos\left(2\omega\tau + \varphi_{q-1} - \varphi_{q+1} + \Delta\varphi_{atomic}\right), \end{aligned} \tag{2.14}$$

where I_q is the intensity of sideband q, ω is the frequency of the IR-field, τ is the delay between XUV and IR, φ_{q-1} and φ_{q+1} are phases related to the XUV-field, $\Delta\varphi_{atomic}$ is the atomic phase, $M_{q\mp1}^{\pm}$ are the two-photon transition amplitudes for harmonic $(q \mp 1)$ and superscript $(\pm)$ indicates if an IR-photon is absorbed $(+)$ or emitted $(-)$. [4] By scanning delay τ, the phase between the XUV and IR is altered, leading to oscillations in the sideband signal with frequency 2ω.

The interference amplitude and phase obtained using the RABBIT protocol provides a complete characterisation of the electron wave packet, provided that it is in a pure state. [12] Meaning that the state can be described with a wavefunction. However, if the photoelectron is in a mixed state, the quantum state can not be described with a wavefunction. Instead, the more general description of the density matrix is needed and therefore also another measuring technique. One method to perform such measurements is quantum state tomography. The method is based on preparing many copies of the same state and perform projective measurements on the state. One scheme for performing this kind of measurements is the KRAKEN protocol.

2.3.2 KRAKEN

The KRAKEN protocol uses a similiar setup to that of the RABBIT protocol. However, in RABBIT we study the interference between two-photon transitions of two consecutive harmonics, while in KRAKEN we study the interference between different two-photon transitions related to the electron wave packet created by absorption of a single harmonic. An illustration of the KRAKEN protocol is shown in Fig. 2.5.

After the atom has been ionised by an incident XUV pulse with central frequency Ω as shown in Fig. 2.5, the photoelectron is probed by two narrowband, spectrally separated and synchronised IR pulses. Since the XUV pulse has a broad bandwidth, denoted $\delta\Omega$ in Fig. 2.5, the photoelectron can occupy a range of continuum states after ionisation, described by the density matrix ρ_E. The two frequency components of the probing arm, ω_1 and ω_2 couple two separate continuum states to the same final state $|\epsilon_f\rangle$, inducing interference.

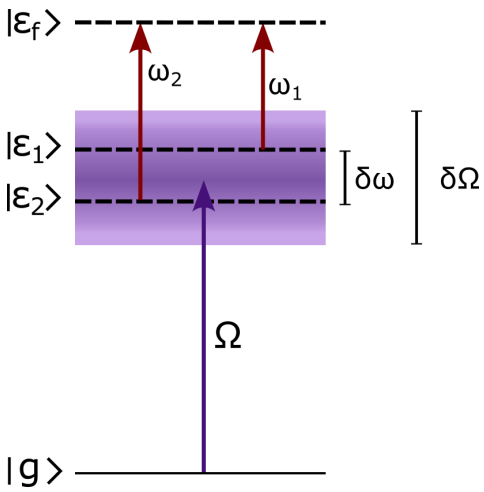

Figure 2.5: Principle of the KRAKEN protocol with an ionising broad band XUV field and transitions driven by a bichromatic IR field.

The probability to find a photoelectron in the final state $|\epsilon_f\rangle$ is given by [8]:

$$\begin{aligned} S(\epsilon_f, \tau, \delta\omega) \approx & \left|M_{\epsilon_f,\epsilon_1}\right|^2 \rho_E(\epsilon_1, \epsilon_1) + \left|M_{\epsilon_f,\epsilon_2}\right|^2 \rho_E(\epsilon_2, \epsilon_2) \\ & + e^{i\delta\omega\tau} M_{\epsilon_f,\epsilon_1} M^*_{\epsilon_f,\epsilon_2} \rho_E(\epsilon_1, \epsilon_2) + e^{-i\delta\omega\tau} M_{\epsilon_f,\epsilon_2} M^*_{\epsilon_f,\epsilon_1} \rho_E(\epsilon_2, \epsilon_1), \end{aligned} \tag{2.15}$$

where $M_{\epsilon_f,\epsilon_1}$ and $M_{\epsilon_f,\epsilon_2}$ are dipole transition matrix elements, ρ_E is the reduced density matrix of the photoelectron, $\delta\omega = \omega_2 - \omega_1$ is the frequency difference between the probe components and τ is the delay between XUV and IR. The first two terms are related to the populations, the main diagonal of the density matrix, and the third and fourth terms are related to the coherences, the subdiagonal elements of the density matrix. In KRAKEN the dipole transition matrices $M_{\epsilon_f,\epsilon_1}$ and $M_{\epsilon_f,\epsilon_2}$ are assumed to be independent of energy across $\delta\Omega$. [8]

The last two terms of Eq. (2.15) depend on the delay τ between the XUV pulse and the IR pulse as well as on the frequency difference $\delta\omega$ between the bi-chromatic IR probe pulse components. In the KRAKEN protocol, the delay between the XUV pulse and the bichromatic IR pulse is varied in order to find the oscillation originating from $\delta\omega$. In a similar way to that of the RABBIT protocol described earlier, the probability to find the photoelectron in the final state $|\epsilon_f\rangle$ oscillates as a cosine-function depending on the delay τ with frequency $\delta\omega$. The Fourier-transform of Eq. (2.15) along delay oscillating at frequency $\delta\omega$ is proportional to:

$$\mathscr{F}\{S(\epsilon_f, \tau, \delta\omega)\}(\delta\omega) \approx M_{\epsilon_f,\epsilon_1} M^*_{\epsilon_f,\epsilon_2} \rho_E(\epsilon_1, \epsilon_2). \tag{2.16}$$

By isolating this component, as a function of final energy ϵ_f, a subdiagonal corresponding

to $\rho(\epsilon_1, \epsilon_2) = \rho(\epsilon_1, \epsilon_1 + \hbar\delta\omega)$ of the reduced density matrix is reconstructed. The subdiagonal, or coherence, is shifted by energy $\hbar\delta\omega$ with regards to the main diagonal. By doing several measurements with different probe fields, different subdiagonals can be determined. [10] In principle, this can be done with an arbitrary number of different $\delta\omega$, allowing to reconstruct the density matrix with increasing resolution. The KRAKEN protocol was first implemented experimentally in [13], where six sub diagonals and the main diagonal were measured separately and the continuous variable density matrix was obtained using a Bayesian estimation algorithm that retrieved the most likely density matrix given the measured partially reconstructed density matrix.

Since KRAKEN relies on measuring one subdiagonal at a time, it is very time consuming to reconstruct the density matrix. Also, since the kinetic energy of each photoelectron is a continuous variable, in principle, an infinite number of measurements would be required to fully map out the density matrix. To improve on the concept of KRAKEN in order to acquire more subdiagonals from a single scan, we introduce the concept of poly-KRAKEN below.

2.3.3 Poly-KRAKEN

The difference between the KRAKEN protocol described above and the new proposed poly-KRAKEN protocol is that poly-KRAKEN utilises more than two spectral components in the probe. The transitions involved in a three and four frequency poly-KRAKEN experiment are shown in Fig. 2.6. The idea is that, by introducing more frequencies, multiple coherences can be encoded in a single spectrogram.

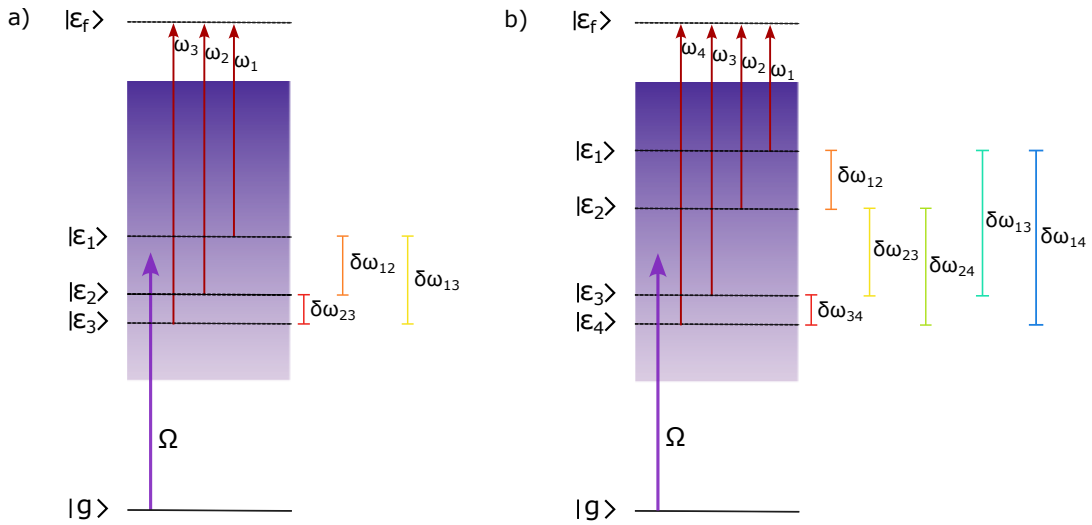

Figure 2.6: An illustration of the transitions that are involved in a three frequency a) and four frequency b) poly-KRAKEN experiment. The beating frequencies for both cases are shown to the right in each figure.

With the configuration shown in Fig. 2.6(a), one more spectral component is added compared to the regular KRAKEN protocol. This extra spectral component allows for a third path to the final state $|\epsilon_f\rangle$, resulting in a total of three beating frequencies $\delta\omega_{12}$, $\delta\omega_{13}$ and $\delta\omega_{23}$, where the indexes represent the involved spectral components. By adding another spectral component, we get six beating frequencies, shown in Fig. 2.6(b).

By increasing the number of beating frequencies, we find more off diagonal components from the Fourier transform of the signal compared to only one component in Eq. (2.16). With four spectral components, and therefore a total of six beating frequencies, there are six components to be extracted from the Fourier transform as:

$$\mathscr{F}\{S(\epsilon_f, \tau, \delta\omega)\}(\delta\omega_{ij} = \omega_j - \omega_i) \approx M_{\epsilon_f,\epsilon_i} M^*_{\epsilon_f,\epsilon_i+\delta\omega_{ij}} \rho_E(\epsilon_i, \epsilon_i + \hbar\delta\omega_{ij}), \tag{2.17}$$

with i and j being the spectral components and $\delta\omega_{ij}$ the beating frequencies shown in Fig. 2.6(b).

Golomb ruler

To get the beating frequencies equally spaced, we use Golomb rulers. A Golomb ruler describes a configuration to put integer points in, such that each pairwise separation is unique. The Golomb ruler for three and four points are shown in Fig. 2.7(a) and (b). As can be seen in (a), by placing the points in this order, separations 1, 2 and 3 can be obtained. In a similar way, separations 1, 2, 3, 4, 5 and 6 can be obtained with a ruler of order four, as shown in Fig. 2.7(b). There exist Golomb rulers of higher degrees as well, however, after order four the rulers are not unique and multiple different configurations are available. [14] A figure of the amount of uniquely defined separations of the first six Golomb rulers are plotted as function of ruler order in Fig. 2.7(c). As shown, the amount of unique separations of the ruler increases much faster than the order, allowing to increase the amount of beating frequencies rapidly with increasing number of spectral components. This results in even more coherences encoded in the spectrogram.

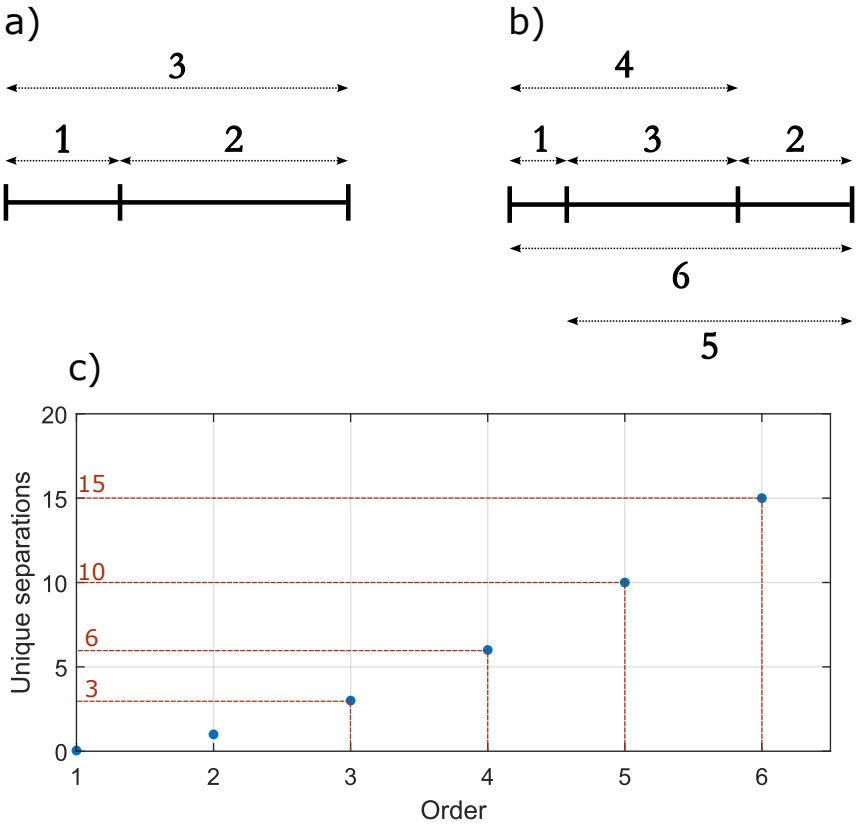

Figure 2.7: An illustration of the Golomb ruler for a) order three with three unique separations and b) order four with six unique separations respectively. In c) the amount of unique separations of the six first Golomb rulers are plotted as function of order.

Chapter 3

Experimental setup

3.1 Experimental setup

3.1.1 Laser

The laser used for the experiments is a Ti:Sa laser with a 25 fs pulse duration, an energy of 5 mJ per pulse and a central wavelength of 800 nm. To create the high energy short pulses, the method of chirped pulse amplification is being used. A short pulse is created in an oscillator, it then gets stretched, amplified and finally compressed. This method is used to be able to amplify a short pulse without damaging the amplifier due to self focusing. [15] An overview of the different components that build up the laser is shown in Fig. 3.1.

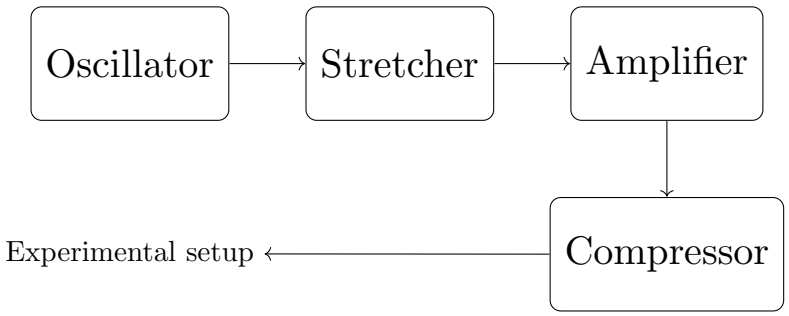

Figure 3.1: An illustrative overview of the laser system used for experiments.

3.1.2 Setup

The setup used for the experiment is shown in Fig. 3.2. This setup has historically been used for doing both RABBIT measurements as well as KRAKEN measurements. Flip mirrors are placed in the pump and probe arm to change between the setup for RABBIT

and KRAKEN. However, in Fig. 3.2 and in the following description, only the parts necessary for KRAKEN measurements are explained in detail.

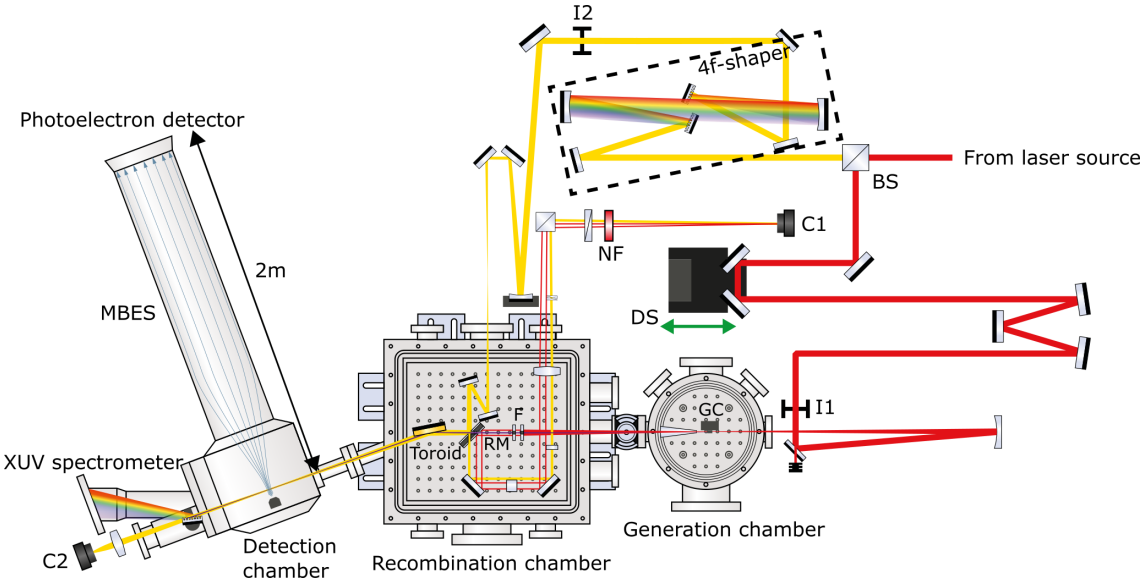

Figure 3.2: An illustration of the setup in the laboratory. The following acronyms are used: BS: beamsplitter, DS: delay stage, GC: gas cell, F: filter, RM: recombination mirror, NF: narrow bandpass filter, MBES: magnetic bottle electron spectrometer, I1 and I2: irises, C1 and C2: cameras. The yellow lines illustrate the probe arm, and the red lines illustrate the pump arm. Figure adapted from [16].

The laser from the source enters the setup in the upper right corner in Fig. 3.2. The first component the beam hits is the beam splitter (BS) where 60% of the intensity is directed to the probe arm, shown as the yellow beam, and 40% is directed to the pump arm, shown as the red beam.

In the probe-arm, the beam is sent to a 4f-shaper. The 4f-shaper is used to spectrally filter certain components of the spectrum of the fundamental laser field. It is described in more detail later in Sec. 3.1.3.

In the pump-arm, the beam is sent on to a retroreflector. The retroreflector consists of two mirrors angled at 90 degrees compared to each other, mounted on top of a motorised delay stage (DS). This delay stage is new and it was installed in the setup as part of this project. The delay stage is used to control the delay between the two arms. After the delay stage the beam is focused into a pulsed gas cell inside the generation chamber, where high harmonics are generated. In this project argon was used as generation gas. After the generation cell, the beam enters the recombination chamber. An overview of the most important components inside the recombination chamber are shown in Fig. 3.4 together with camera (C1) as also shown in figure Fig. 3.2. In the recombination chamber, the

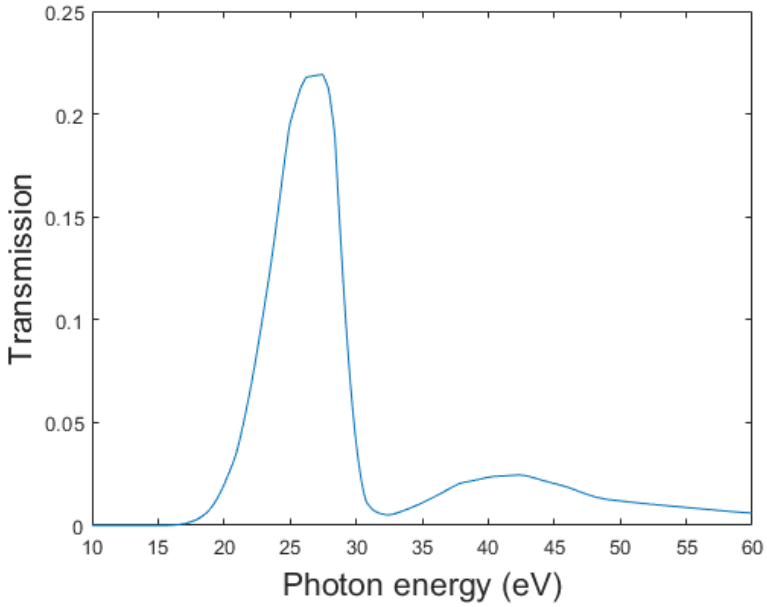

Figure 3.3: The transmission curve for the AlGe-filter mounted on the filterwheel (FW).

beam hits a filter (F) that removes the middle part of the IR-field and attenuates some of the higher harmonics. The filter is shown to the right in Fig. 3.4, with a central part and an outer part. In this project a filter with an outer part of fused silica and an inner part composed of aluminium and germanium was used. The transmission curve of the filter used is shown in Fig. 3.3. The filter attenuates harmonics that are outside of the region of $23 - 29\,\mathrm{eV}$, minimising the contributions from higher harmonics to the sideband of interest.

At this point, the pump and the probe arms are recombined. They both hit the recombination mirror (RM), illustrated in Fig. 3.4. The pump beam with an outer IR part and an inner XUV part hits the mirror from right, transmitting the XUV light through the hole and reflecting the IR downwards. The probe beam hits the mirror from above in Fig. 3.4, reflecting the outer parts of the light to the left and transmitting the middle part downwards. The parts of the beam that propagates to the left in Fig. 3.4 then hit a toroidal mirror and gets focused into a gas jet in the detection chamber. This is where the photoionisation used for the KRAKEN experiments take place. In this project argon was used as detection gas. The parts of the beam that after the recombination mirror propagates downwards in the figure gets focused down on a camera (C1) outside of the chamber. When the IR from probe and pump overlap temporally on the camera, a fringe pattern (FP) can be observed, see Fig. 3.4. The fringe pattern is used as a reference for controlling and stabilising the delay between both arms, as described further in Sec. 3.1.4.

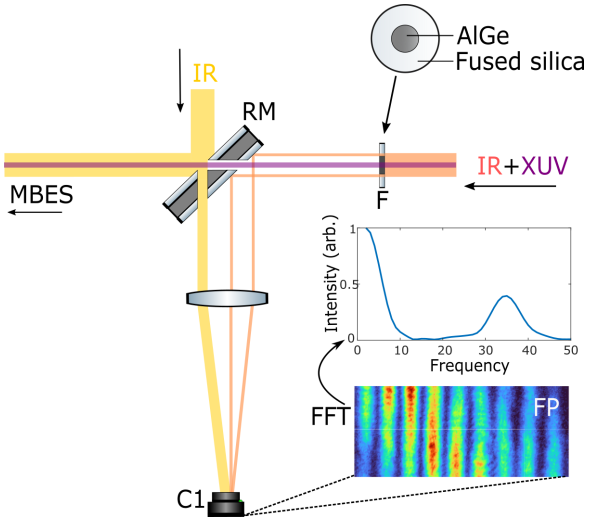

Figure 3.4: A view of the most important parts of the recombination chamber from above. The camera used for measuring delay is shown together with the fringe pattern due to overlapping probe and pump beams. Figure adapted from [16].

3.1.3 Spectral filtering

The 4f-shaper as shown in Fig. 3.2 and in a more zoomed in version in Fig. 3.5 is used to separate the spectral components of the fundamental laser in space. This is indicated by the multiple colours in Fig. 3.5. The beam is separated by first being reflected on a grating (G1). The beam is then reflected on a focusing mirror (FM1) with focal length f at a distance f from the grating, that focuses the different spectral components at different positions in the focal plane. In the setup, the focal plane is situated just above two gratings (G1) and (G2). A second mirror (FM2), positioned at a distance f from the focal plane collimates the individual spectral components. Finally, a second grating (G2) at a distance f from (FM2) is used to ensure that the different spectral components propagate in the same direction. By inserting a blocking mask in the focal plane as shown in Fig. 3.5 the spectrum of the light transmitted through the 4f-shaper can be manipulated..

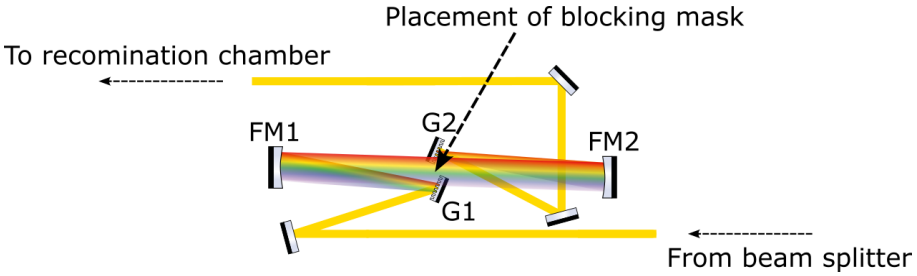

Figure 3.5: The 4f-shaper used for spectrally filtering the probe arm.

For the poly-KRAKEN experiment a mask using four slits is inserted in the focal plane in

order to obtain four spectral components in the IR pulse. The slits are cut according to the Golomb ruler of order four and length six. An illustration of the blocking mask with four slits is shown in Fig. 3.6.

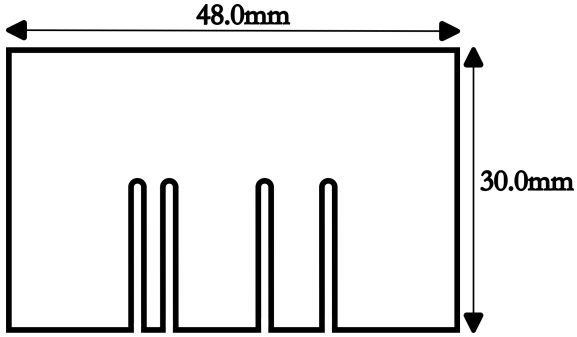

Figure 3.6: A blocking mask with four slits cut according to the Golomb ruler of length six.

A picture of the 4f-shaper with the slits installed is shown in Fig. 3.7. The photo is taken from above mirror (FM2), after the focal plane. The blocking mask is mounted on a manual stage that can move the blocking mask horizontally inside the focal plane to select frequency components. The manual stage is mounted on to a construction above the 4f-shaper. As this project was done in parallel with another master thesis student, Gustav Arvidsson, we came up with a solution allowing to easily insert the blocking mask in to the focal plane of the 4f-shaper by manually loosening a bolt and put the slits at the correct placement. The mount of the blocking mask also allows to easily change to a different blocking mask in case a different slit configuration is desired.

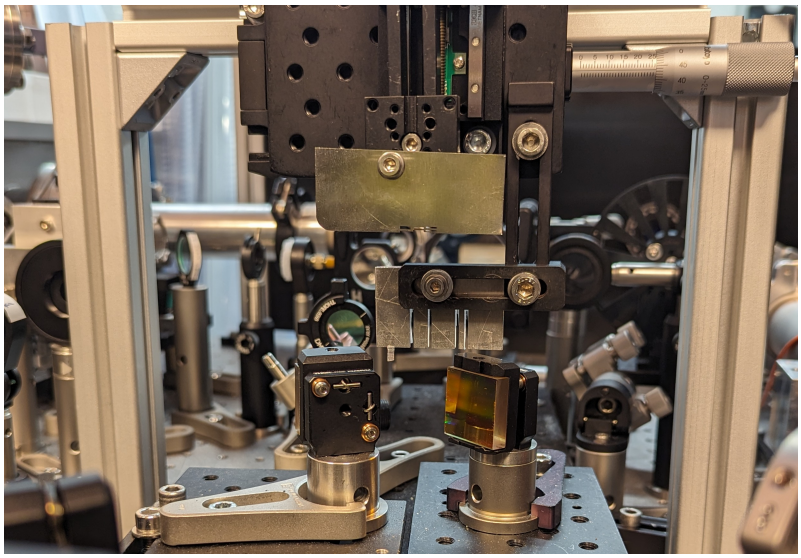

Figure 3.7: A picture of the 4f-shaper with a blocking mask installed in the focal plane.

An example of both the fundamental spectrum as well as the filtered spectrum is shown in Fig. 3.8. Here, the blocking mask in Fig. 3.6 is inserted in to the focal plane, resulting in the transmission of four narrow-width spectral components.

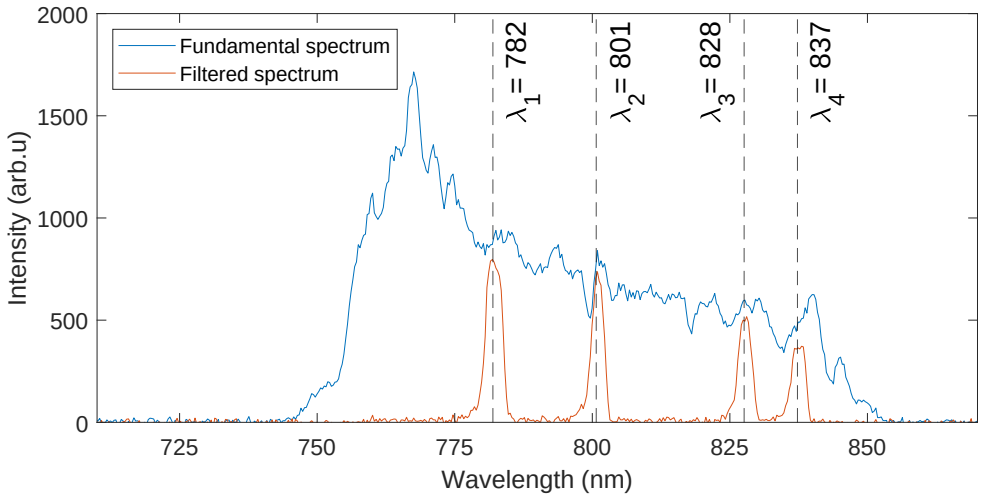

Figure 3.8: An example of the spectrum of the probe measured with and without blocking mask. The peaks of the filtered spectrum are named according to the spectral component it corresponds to in poly-KRAKEN.

3.1.4 Delay scan

To perform a scan and measure the photoelectron spectrum at different delays, the delay stage (DS) is used. When performing RABBIT scans, the beating frequency as a function of delay of the sideband signal is 2ω, see Eq. (2.14). With a fundamental field with central wavelength 800 nm, this corresponds to a beating period of $T = \frac{2\pi}{2\omega} = 1.33\,\text{fs}$. However, for performing KRAKEN scans, the beating frequencies are given by $\delta\omega$. Depending on which spectral components that are selected in the 4f-shaper, the beating frequency varies. By considering the example probe spectrum in figure Fig. 3.8, the lowest beating frequency is related to the two right most peaks, λ_3 and λ_4. Here we get a beating frequency of around $\delta\omega = \frac{2\pi c}{\lambda^2}\delta\lambda = 3.89\,\text{THz}$ which gives a beating period of $T = \frac{2\pi}{\delta\omega} = 257\,\text{fs}$. The fastest beating frequency is related to the two outer most peaks, λ_1 and λ_4, which corresponds to a beating frequency of $\delta\omega = 25.2\,\text{THz}$ and beating period of $T = 39.7\,\text{fs}$. This puts a constraint on the step size that can be used during experiments, where the step size can maximally be half that of the lowest beating period in order to resolve all components. However, in order get a good resolution of the beating frequencies, the scan has to be done over multiple periods of the signal, which is, as can be seen from above, much longer than for RABBIT experiments. In order to be able to scan sufficiently long to distinguish the beating frequencies of the poly-KRAKEN scan, a new controllable stage with a longer

range had to be implemented in to the setup. The new stage is an electronic linear stage made by the company Zaber with model name X-LDA025A-AE53D12. It has a travel range of 25 mm, allowing to scan over a total delay of $2 \times 25\,\mathrm{mm}/c = 166.782\,\mathrm{ps}$. The old stage used for scanning had a range of $2 \times 100\,\mu\mathrm{m}/c = 0.668\,\mathrm{ps}$. The factor of two is added since we reduce the beam path length both before and after the reflection of the retroreflector on the delay stage.

To control the new stage, I implemented it in the LabView-program used for scanning and controlling the delay of the setup, here mentioned as the stabilisation program. LabView is used for controlling multiple parts of the setup, with the delay and stabilisation being one of them. The new stage uses a different communication protocol compared to that of the old stage and therefore I had to modify the stabilisation program. A switch was added to the program to allow for switching between using the old stage and the new stage. The new stage was therefore installed alongside the old stage, and all the functionality was kept. An image of the stabilisation program is shown in Fig. 3.9.

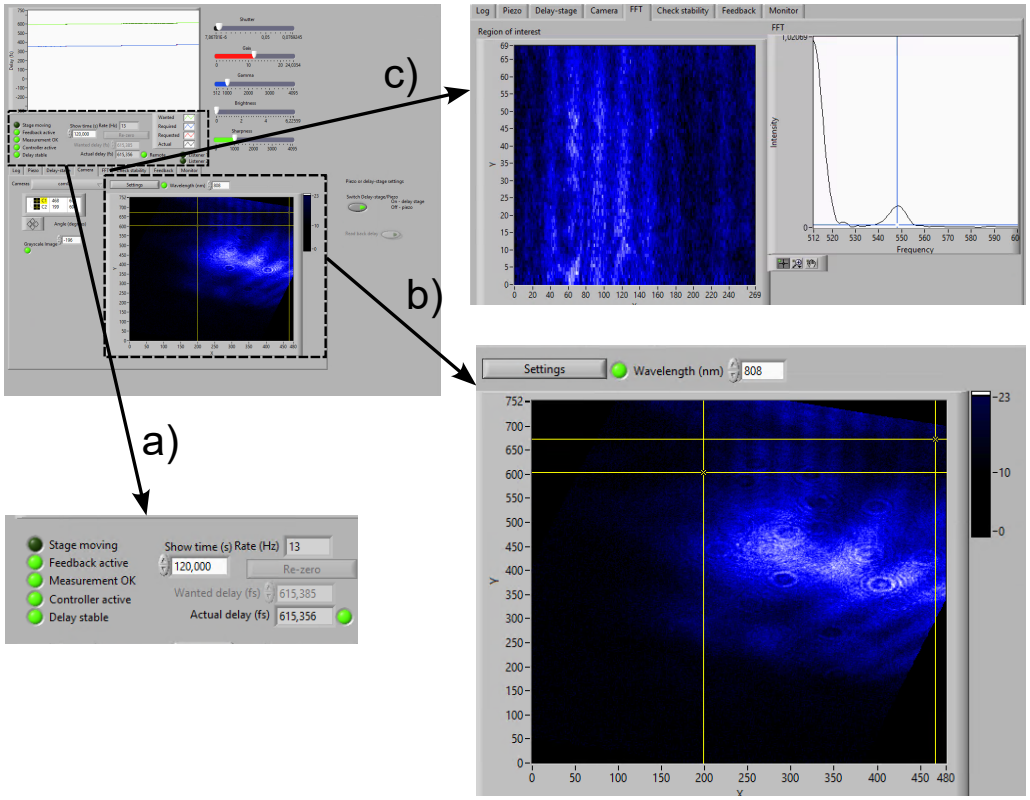

Figure 3.9: An image showing the stabilisation program during a scan. The three most important parts are: a) indicators for stabilisation and delay measurement, b) the fringe pattern measured using camera (C1) in Fig. 3.4 and c) the FFT of the yellow boxed area of the fringe pattern in b).

In Fig. 3.9(b), the image of camera C1 is shown. In Fig. 3.2, before the beam hits camera (C1), it passes through a narrow bandpass filter (NF). The bandpass filter only lets through light with wavelengths within 10 nm of the specified wavelength. This results in an elongation of the temporal profile of the pulses. This allows to have partial temporal overlap for a larger range of delays, allowing to actively stabilise the delay over approximately 1 ps. The yellow lines on the image are used to choose an area where the fringe pattern is apparent. The FFT (Fast Fourier transform) of the fringe pattern within the selected area, shown in Fig. 3.9(c) is computed and used to determine the phase of the fringes. When the phase is known, the relative delay between the two arms can be determined. The relative delay is shown as "Actual delay (fs)" in Fig. 3.9(a). It is important to make sure that we move the delay stage slow enough so that the camera can track the phase variation. If the phase varies too quickly, the camera is not able to resolve it and the delay reference is therefore lost. This leads to the stage moving a larger distance than specified.

By continuously measuring the phase and comparing the actual delay to the wanted delay, a feedback loop with a PID-controller is used to stabilise the delay. After installing the new stage, the PID-controller had to be adjusted. I tested different parameters and found that $P = 0.2$, $I = 6$ and $D = 0$ gave the best result. Additionally, the maximum rate at which the stage is allowed to move with was increased. With these adjustments a short term stability of around 50 as was achieved. This program is not only used for stabilisation, but also to move the stage to perform measurements at different delays. By changing the wanted delay, shown in Fig. 3.9(a), the stage will move to adjust the actual delay.

3.2 Experiment

3.2.1 Controlling the setup

As mentioned earlier, the computer program LabView is used for controlling the setup during measurements. It is mainly used for two things: to control and stabilise the delay (as described in the previous section), and to acquire the photoelectron spectrum from the MBES shown in Fig. 3.2. This is done with three programs of LabView. A schematic of the three programs and their interactions is shown in Fig. 3.10.

The scan program is the main program used during scans. In this program, the experimental parameters: total delay distance, delay step size and acquisition time are set. During a scan the program communicates with the stabilisation program to move the delay according to the preset parameters. At each delay step, the acquisition program collects the photoelectron spectrum for the time set as acquisition time. After the acquisition time has passed, the photoelectron spectrum is saved and the scan program sends a signal to

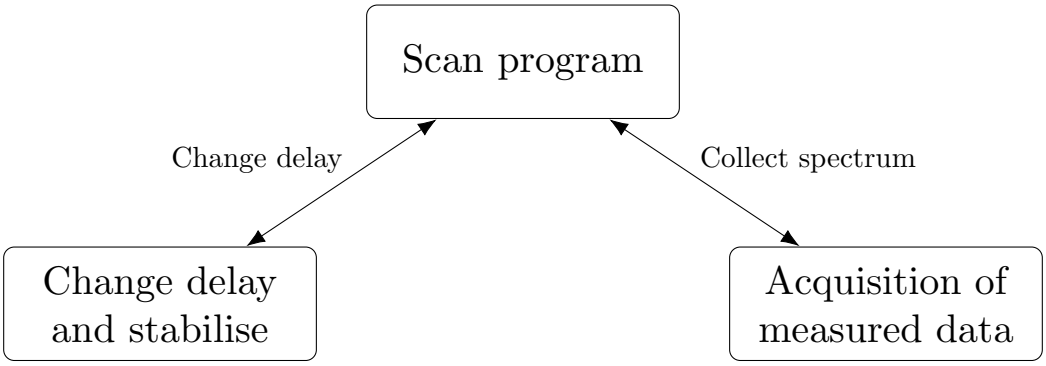

Figure 3.10: An overview of the LabView programs and their interactions.

the stabilisation program to move the delay stage to the next delay step. When the stage has moved, a new acquisition of photoelectron starts. This process is repeated until the stage has moved the total delay distance specified above.

3.2.2 Data collection

The data measured during an experiment is the time-of-flight photoelectron spectrum for each delay step and the spectrum of the probe-arm.

Photoelectron spectrum

During a scan, the photoelectron spectrum is measured using the MBES in Fig. 3.2. In the detection chamber a jet of atoms is intersected with the beam of the XUV field. The XUV field ionises the atoms and the resulting photoelectrons are guided along the MBES tube by magnetic fields. The magnetic field is designed to collect the photoelectrons emitted in all directions allowing a high detection efficiency. At the end of the MBES the photoelectrons are detected.

The time-of-flight is determined by two signals. In the beginning of the setup, a photodiode is mounted. When a laser pulse hits the photodiode, a start signal is generated. Then the pulse propagates through the setup and ionises atoms in the detection chamber. When the resulting photoelectrons hit the detector, after travelling down the MBES tube, a stop signal is generated. The difference between start signal and stop signal is the time-of-flight of the photoelectrons.

However, we want the photoelectron spectrum as a function of kinetic energy. To convert the measured time-of-flight to kinetic energy, the following formula is used:

$$E_k = \frac{m_e}{2}\left(\frac{L+\gamma}{t_{ToF}}\right)^2, \tag{3.1}$$

where m_e is the electron mass, L is the length of the MBES tube, γ is a calibration parameter and t_{ToF} is the measured time-of-flight. [17]

Probe spectrum

The spectrum of the probe arm is measured using a spectrometer after the 4f-shaper. By inserting or removing the blocking mask from the focal plane, the spectrum can be measured either in its entirety or after filtering. An example of the probe spectrum and the total fundamental spectrum was earlier shown in Fig. 3.8.

3.2.3 Preparing for a scan

After the laser has been started, the first step is to align the laser to make sure that the beam enters the setup with correct position and angle. This is done by adjusting two mirrors according to two references. After alignment, we can start working on the experimental setup as shown in Fig. 3.2. To start with, we block the probe arm at the beam splitter (BS) and focus on the pump arm.

Firstly, we start the pulsed gas cell (GC). The laser is focused into the gas cell filled with argon, generating XUV radiation. The XUV radiation is measured with the XUV spectrometer mounted at the end of the beamline as shown in Fig. 3.2. By studying the harmonics on the XUV spectrometer, we optimise the position of the gas cell (GC) and the laser intensity using iris (I1). By optimising these parameters we attenuate the intensity of higher harmonics that are not of importance for the experiment.

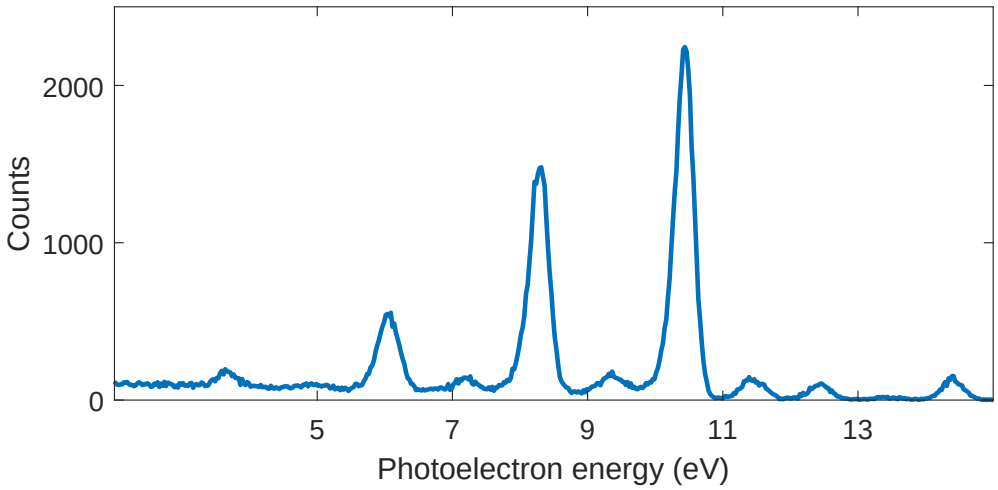

Figure 3.11: Photoelectron spectrum plotted as a function of kinetic energy for a single delay step during a poly-KRAKEN scan. The plot shows

The next step is to start the gas jet in the detection chamber and switch on the photoelec-

tron detector. Then the probe is unblocked and sent through the setup. If the pump and probe are overlapping both spatially and temporally in the detection chamber, two-photon transitions can occur and create a sideband signal. An example of the detected photoelectron spectrum as a function of kinetic energy with both pump and probe apparent is shown in Fig. 3.11. Here the AlGe filter mentioned earlier and the blocking mask with four slits are used. We see three strong one-photon transition peaks at around 6 eV, 8 eV and 10.5 eV as well as a sideband signal in between the peaks and after the strongest peak at 10.5 eV.

Next, we start the stabilisation program shown in Fig. 3.9. We move the stage to find fringes with the strongest contrast. By studying the FFT of the fringe pattern, as shown in Fig. 3.9(c), and optimising its amplitude by moving the delay stage, we can find a rough estimate of the delay value for where the pump and probe overlap temporally.

If at this point, we have any sideband signal in the photoelectron spectrum, we go on to adjusting the recombination mirror (RM) in Fig. 3.4 in order to optimise the sideband signal. Otherwise, if we do not see any sideband signal, we use camera (C2) in Fig. 3.2 to image the foci of the pump and probe in the MBES. The focus of the pump beam is used as a reference and then the recombination mirror (RM) is adjusted to overlap the probe with the reference of the pump.

The final adjustment before starting a scan is to adjust the intensity of the probe beam using iris (I2) to get a sideband signal that is not too strong so that only one IR photon is absorbed or emitted, but strong enough to have a good signal to noise ratio.

Chapter 4

Experimental results and analysis

4.1 Experiments and data

During the time of this project, we acquired a total of 11 poly-KRAKEN scans. For some of the scans no clear sidebands could be observed indicating that the XUV and IR pulses were not properly overlapped spatially or temporally. For other scans sidebands were measured but no oscillations were obsered, possibly due to imperfect alignment of the XUV and IR beams. However, after improving the alignment of the setup, optimising the spatial overlap in the MBES, testing a different slit configuration and optimising the intensity of both probe and pump, a few successful scans were obtained. Here we present only the result from best scan.

The spectrogram of the final scan is plotted in Fig. 4.1(a) with the x axis as the photoelectron energy in unit eV, and the y axis as the pump-probe delay. The main energy interval of interest is the sideband after the strongest one-photon transition. In this spectrogram it corresponds to the sideband at around 11 eV. We focus on this specific sideband because, in this case, the sideband signal is dominated by the contribution of the path involving absorption of one harmonic and absorption of one photon. In contrast, for the other sidebands, the signal results from the interference from two paths corresponding to the absorption of either of the adjacent harmonics and absorption or emisison of an IR photon, complicating the interpretation of the results. A zoomed in version of the sideband of interest is shown in Fig. 4.1(b). We observe clear oscillations as function of delay. The oscillations are irregular, indicating that there may be multiple underlying frequencies, as expected from a poly-KRAKEN scan.

The scan spans a total delay of 1 ps with a step size of 7.69 fs. The acquisition time for each step was one minute and 15 seconds. The delay stability fluctuated around 50 as and the total duration of the scan was just under three hours.

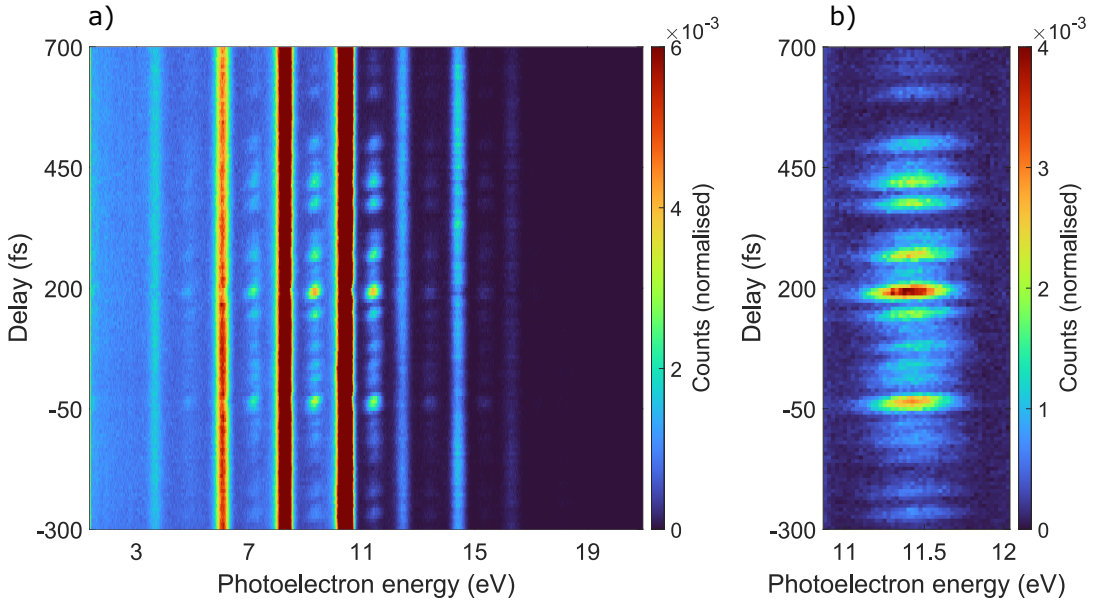

Figure 4.1: A poly-KRAKEN scan plotted with photoelectron energy on x-axis, delay on y-axis and number of counts as the colormap. In a) the complete measured photoelectron spectrogram is shown and in b) only the sideband of interest is shown.

The spectrum of the probe beam that was used for the scan is shown in Fig. 4.2. The red lines illustrate the centre of mass of each peak, which are used to compute the expected beating frequencies. This spectrum is also used to normalise the amplitude for each beating frequency originating from the sideband, which is described in further detail in Sec. 4.2.

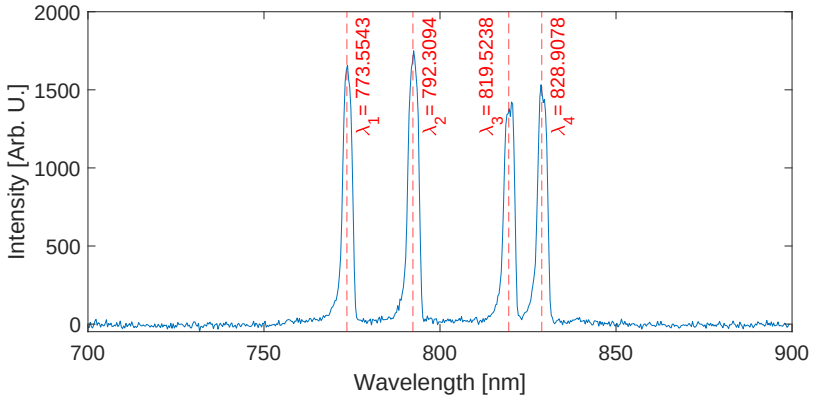

Figure 4.2: The probe spectrum used during the scan. The centre of mass of each peak is marked as a red line and labelled with λ_i.

4.2 Analysis

4.2.1 Fourier analysis of the sideband oscillations

To extract the necessary information to reconstruct the reduced density matrix of the photoelectron, we start by taking the Fourier transform of the spectrogram shown in Fig. 4.1. The modulus of the result is shown in figure Fig. 4.3. In Fig. 4.3(a) the FFT is plotted as a function of photoelectron energy with the positive frequencies on the y-axis and the complete measured photoelectron spectrum in units of energy on the x-axis. The white lines illustrates the expected beating frequencies computed using the probe spectrum in figure 4.2. A zoomed in version of the sideband of interest, at around 11.5 eV, is shown in Fig. 4.3(b).

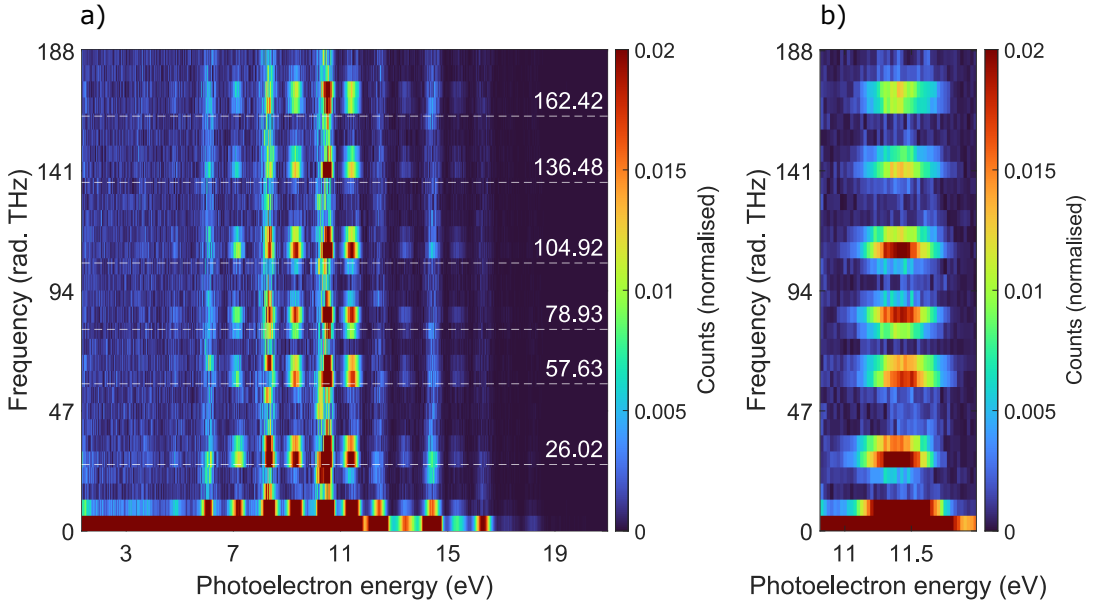

Figure 4.3: The modulus of the FFT of the spectrogram shown in Fig. 4.1 with only the positive frequencies shown. In a) the Fourier spectrum is plotted for every measured photoelectron energy and in b) only the sideband of interest is shown.

Each expected beating frequency $\delta\omega_{ij}$ is computed as the difference between each of the spectral components ω_1, ω_2, ω_3 and ω_4. Since the spectrum is measured as a function of wavelength, we have to convert the differences to frequency. This is done according to the following formula:

$$\delta\omega_{ij} = \frac{2\pi c}{\overline{\lambda}_{ij}^2}\delta\lambda_{ij}, \tag{4.1}$$

where c is the speed of light, λ_i and λ_j are the two spectral components involved in beating frequency $\delta\omega_{ij}$,

$$\delta\lambda_{ij} = \lambda_j - \lambda_i \qquad \text{and} \qquad \overline{\lambda}_{ij} = \frac{(\lambda_i + \lambda_j)}{2}. \tag{4.2}$$

For clarity, the formula for each expected beating frequency and the resulting value is shown in Eq. (4.3).

$$
\begin{aligned}
\delta\omega_{34} = \omega_4 - \omega_3 &= \frac{2\pi c}{\overline{\lambda}_{34}^2}(\lambda_4 - \lambda_3) = 26.02\,\text{rad.THz} \\
\delta\omega_{12} = \omega_2 - \omega_1 &= \frac{2\pi c}{\overline{\lambda}_{12}^2}(\lambda_2 - \lambda_1) = 57.63\,\text{rad.THz} \\
\delta\omega_{23} = \omega_3 - \omega_2 &= \frac{2\pi c}{\overline{\lambda}_{23}^2}(\lambda_3 - \lambda_2) = 78.93\,\text{rad.THz} \\
\delta\omega_{24} = \omega_4 - \omega_2 &= \frac{2\pi c}{\overline{\lambda}_{24}^2}(\lambda_4 - \lambda_2) = 104.92\,\text{rad.THz} \\
\delta\omega_{13} = \omega_3 - \omega_1 &= \frac{2\pi c}{\overline{\lambda}_{13}^2}(\lambda_3 - \lambda_1) = 136.48\,\text{rad.THz} \\
\delta\omega_{14} = \omega_4 - \omega_1 &= \frac{2\pi c}{\overline{\lambda}_{14}^2}(\lambda_4 - \lambda_1) = 162.42\,\text{rad.THz}
\end{aligned}
\tag{4.3}
$$

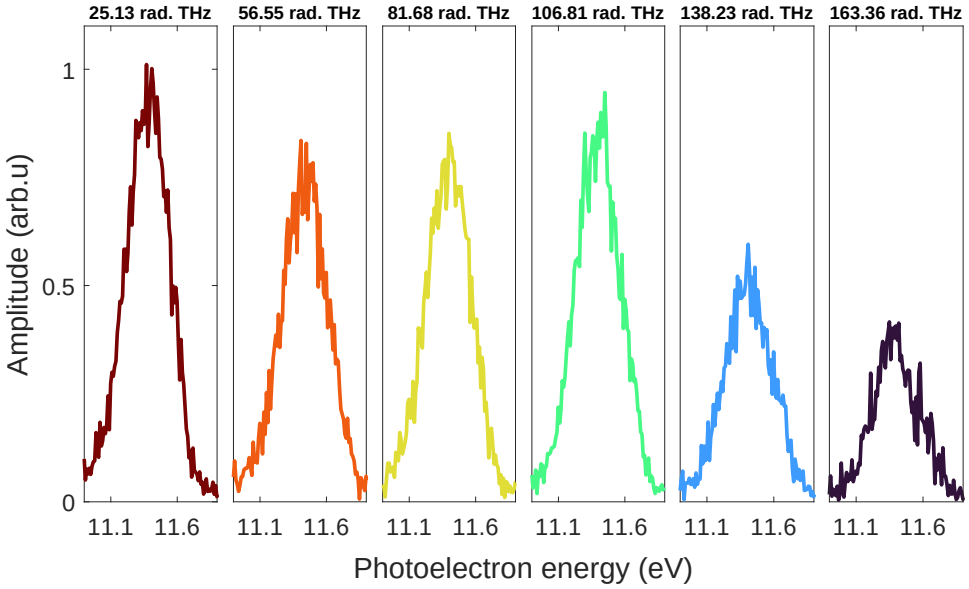

Figure 4.4: The spectral amplitude of the six beating frequencies extracted by FFT.

The next step is to extract the spectral amplitude for each of the beating frequencies. By picking the closest sample to that of the white lines in Fig. 4.3(a), and plotting them separately, we get what is shown in Fig. 4.4. The modulus of the complex spectral amplitude is plotted as a function of photoelectron energy with each beating frequency in a separate graph. The components are proportional to the coherences of the photoelectron

density matrix (see Eq. (2.17)). More specifically, they correspond to specific subdiagonals, positioned at a distance $\delta\omega$ from the main diagonal.

As shown in Eq. (2.17), in order to extract the value of the coherences from the measured amplitudes, it is necessary to account for different strengths of two continuum-contunuum transitions, which are proportional to the amplitude of the different spectral components of the IR field. As a result, the signal is normalised according to:

$$A_{\delta\omega_{kl}} = \frac{A^{raw}_{\delta\omega}}{\sqrt{I_{\omega_i} I_{\omega_j}}}, \tag{4.4}$$

as presented in [13], where $A^{raw}_{\delta\omega}$ is the spectral amplitude of the beating frequency $\delta\omega$ presented in Fig. 4.4 and I_{ω_i} and I_{ω_j} are the integral of peak i and j of the probe spectrum. The six subdiagonal amplitudes after normalisation are shown in Fig. 4.5.

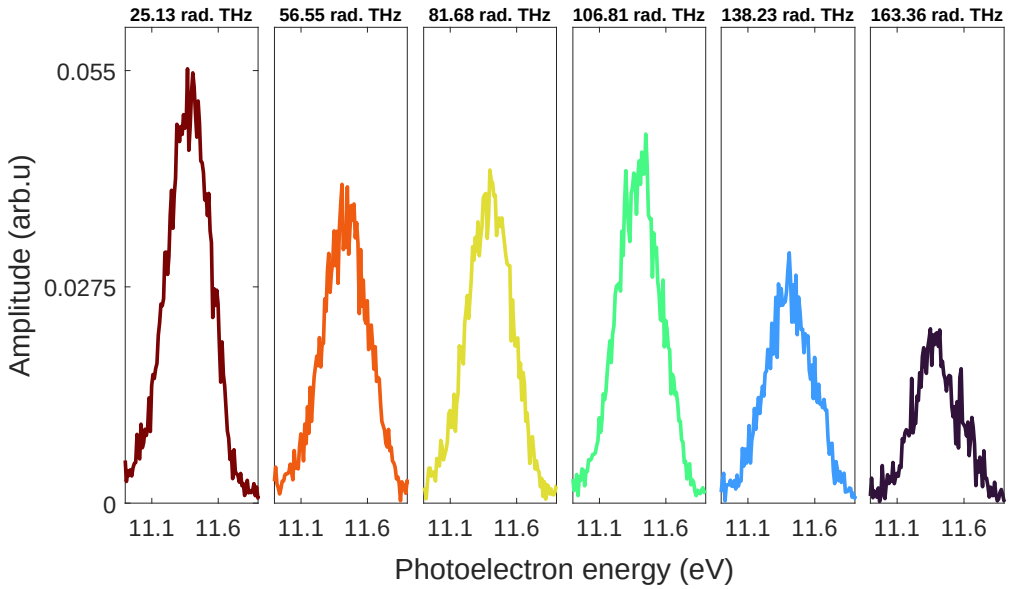

Figure 4.5: The six subdiagonal amplitudes extracted by FFT plotted after normalisation.

4.2.2 Constructing the reduced density matrix amplitude

As can be seen in Fig. 4.3, each beating frequency component occurs at slightly different photoelectron energies. This shift is due to the fact that different parts of the IR spectrum give rise to different beating frequencies, resulting in a different central IR photon energy for each spectral component.

This energy offset must be corrected before inserting the subdiagonals in the initially

empty density matrix. To do so, we shift each subdiagonal down with energy:

$$E_{shift} = \frac{hc}{\overline{\lambda_{ij}}}, \tag{4.5}$$

where h is the Planck constant, c is the speed of light and $\overline{\lambda_{ij}}$ is the central wavelength as described in Eq. (4.2).

A plot containing all subdiagonals after being shifted is shown in Fig. 4.6.

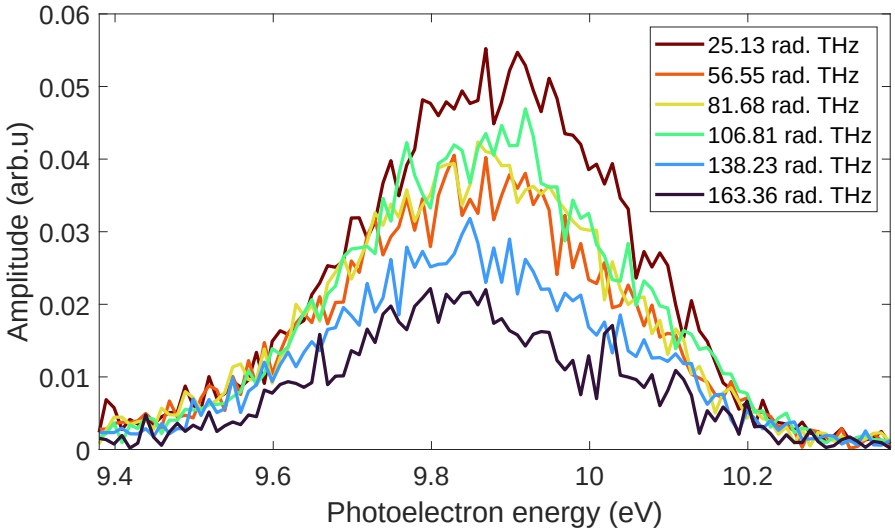

Figure 4.6: Each subdiagonal plotted after being shifted by the energy corresponding to the central wavelength of the probe spectrum for that beating frequency.

After shifting all subdiagonals to the correct photoelectron energy, the reduced density matrix of the photoelectron is constructed. Each subdiagonal is inserted into the empty matrix with its offset to the main diagonal decided on according to its beating frequency $\delta\omega_{ij}$. The procedure is then repeated for the lower subdiagonals, with negative frequency $-\delta\omega_{ij}$. The final reconstructed reduced density matrix for the photoelectron is shown in Fig. 4.7. As can be seen, the reduced density matrix has an elliptical shape, with the main axis of the ellipse being along the diagonal. The fully coherent photoelectron quantum state would be characterised by a density matrix amplitude that is fully circular. The elliptical shape of the density matrix indicates that the photoelectron quantum state is only partially coherent. The loss of coherence is mainly due to two reasons: the response function of the photoelectron detector as shown in more detail in [13] and the spin-orbit splitting of the ionic ground state of argon. Due to the spin-orbit splitting, the ionisation potential is different depending on the state of the related ion, which results in an incoherent superposition of two photoelectron states centred at different energies, spaced by

the spin-orbit splitting (180 meV in argon). This is shown in Eq. (2.13), where the two density matrices related to the ionic states $\left|j=\frac{1}{2}\right\rangle$ and $\left|j=\frac{3}{2}\right\rangle$ are added incoherently to create the total reduced density matrix. However, in Fig. 4.4 to Fig. 4.7, it is clear that the two states can not be resolved due to insufficient spectral resolution. It is interesting to note that in principle, if the XUV pulses were very broad, it would also not be possible to resolve the spin-orbit splitting. However, if we measure the density matrix, these two cases will lead to different density matrices. In the case when we are limited by spectrometer resolution we will get experimental decoherence and the density matrix will be elongated along the diagonal, on the contrary, in the case of very broad XUV pulses, the density matrix would be close to circular [8], which is not the case here.

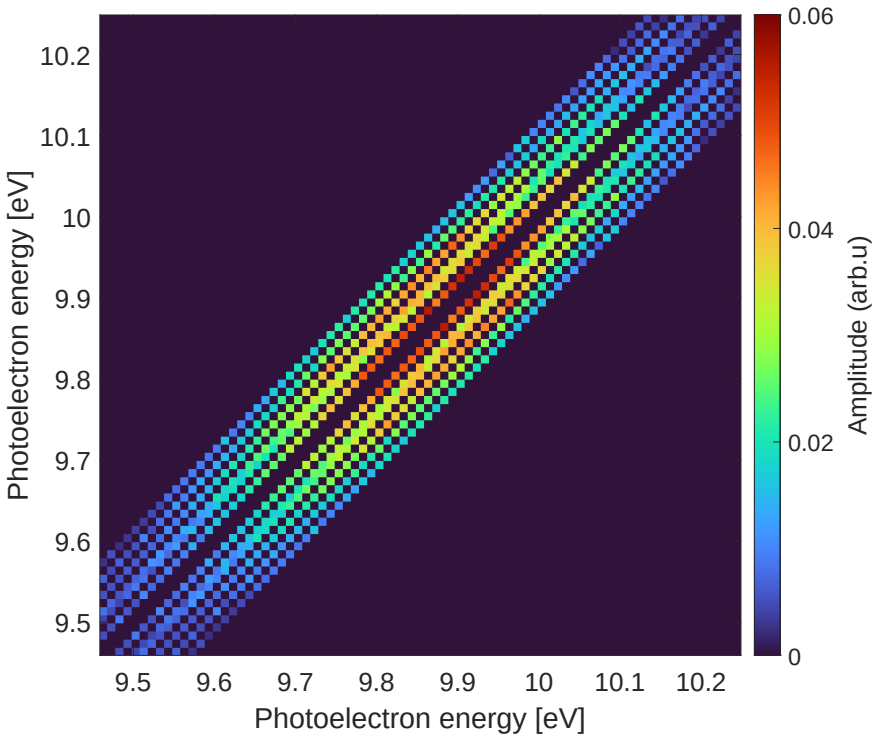

Figure 4.7: The reconstructed reduced density matrix amplitudes using the poly-KRAKEN protocol.

4.2.3 Effect of the coherence properties of the IR pulses

The second best scan we did showed clear beating frequencies. However, when analysing the data from this scan we realised that the probe spectrum measured using the spectrometer was not enough to normalise according to Eq. (4.4). By taking the FFT of the spectrogram of the scan, it was clear that the beating frequencies related to the outer parts of the probe spectrum had a significant lower amplitude than expected. After normalising

according to the probe spectrum, this was still the case. We think that this could be due to the fact that some of the outer parts of the fundamental spectrum, especially for the lower wavelengths, has a contribution of incoherent light. This could come from the process of amplified spontaneous emission (ASE), arising from the laser amplifier. The gain medium in the laser generates photons via spontaneous emission which are then amplified. [18] This light is not coherent with the main pulse, and does not contribute to the two-photon transitions. Using a spectrometer, it is not possible to disentangle the contribution from coherent and incoherent parts. If a peak in the probe spectrum has a large part that is incoherent light, we are overnormalising. This situation is illustrated in figure Fig. 4.8. Here it is clear that some amplitudes are very small, probably due to this effect which is particularly strong for the outer parts of the spectrum.

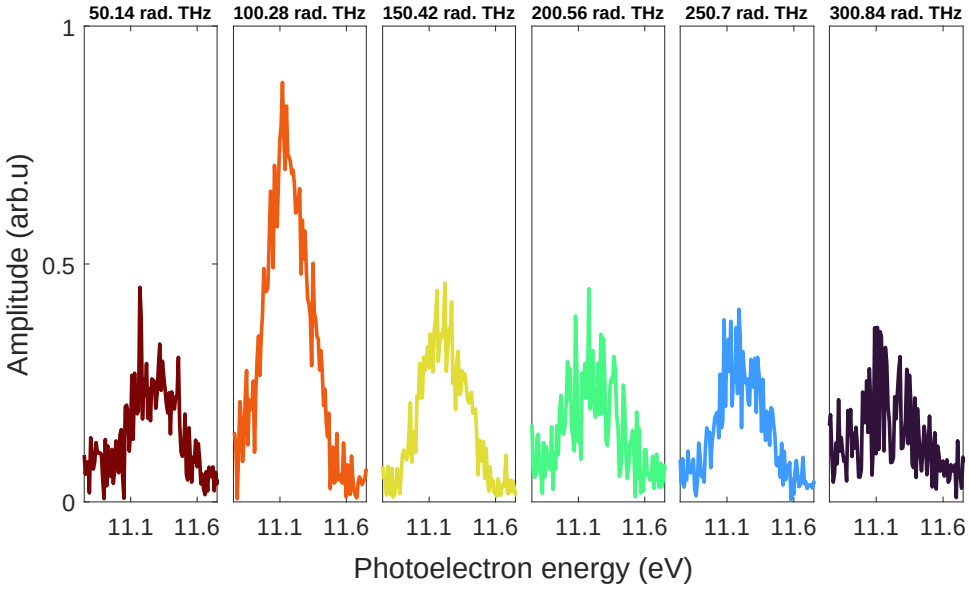

Figure 4.8: The six subdiagonal amplitudes extracted from the FFT plotted after normalisation for a different scan than the one presented in the results part.

This led to the idea to design a new blocking mask with slits that are less separated, allowing us to avoid the outer parts of the spectrum. The old blocking mask had a distance of 2.8 mm from the left most slit to the right most slit. The corresponding distance for the new slits is 2 mm. The scan result with the new slits is the result presented in Fig. 4.1.

Chapter 5

Conclusion and outlook

5.1 What did I do?

Experimentally, in this project, I have been working on implementing the new delay stage and modifying the delay stabilisation software accordingly. I have also designed the new blocking mask that we used for the scan presented in the result section of this report. I performed the experiments together with PhD students. I was responsible for the data analysis, where I used programming code that was available from previous experiments to load the data and I modified it to analyse our specific experiments.

5.2 Conclusion

In this project, a new measurement protocol for performing quantum state tomography on photoelectrons has been implemented experimentally. By building on the concept of the KRAKEN protocol, the poly-KRAKEN protocol was introduced with the benefit of being able to extract multiple coherences from a single scan. By increasing the amount of spectral components of the probe field, a larger amount of different two-photon transitions could occur and hence more beating frequencies appear. In order to implement the poly-KRAKEN protocol, the experimental setup was modified by implementing a new motorised delay stage. The new delay stage has a longer range, allowing for scanning over a delay of multiple picoseconds, compared to the old stage with a range of 0.6 picoseconds. A new blocking mask for the 4f-shaper was designed to pick out spectral components closer to each other, minimising the contribution of non-coherent parts of the fundamental spectrum.

The experiments were performed in argon atoms. By measuring the photoelectron spectrum at different time delays between XUV and IR, a spectrogram of photoelectron spectra

as function of delay was acquired. The sideband signal exhibited an oscillatory pattern with six different beating frequencies. To reconstruct the reduced density matrix amplitude of the photoelectron, the beating frequencies were extracted from the FFT of the spectrogram. Since the beating frequencies of the spectrogram are proportional to the subdiagonals of the reduced density matrix, the matrix was partially reconstructed. The resulting reduced density matrix shows an elliptical pattern that indicates that the photoelectron quantum state is partially coherent. This observation can be attributed to two different effects. First, spin-orbit splitting of the ionic state of argon results in entanglement between the ion and the photoelectron. As a result, if only the photoelectron is measured, its reduced photoelectron quantum state is characterised by a statistical mixture. Second, the limited spectral resolution results in a broadening of the photoelectron spectra that leads to an elongation of the subdiagonal, effectively introducing an experimental source of decoherence.

5.3 Outlook

One area for development is to increase the amount of slits in the blocking mask, to increase the amount of spectral components of the probe. During this project we used four slits. This could in principle be increased to an arbitrary amount of slits within the limitations of fitting them inside the spectrum of the 4f-shaper. By increasing the number of slits, more beating frequencies, and therefore, more subdiagonals will be obtained from a single scan.

Adding more slits would require scanning over a longer delay range in order to reach high enough spectral resolution in the Fourier transform to resolve all the beating frequencies. One limitation that restricted us from scanning over a longer total delay range, was the decrease in fringe pattern contrast in the stabilisation program for delays farther than 500 fs away from the maximum. By installing a new narrower bandpass filter before camera C1, the pulses could be even more elongated, resulting in a larger overlap region for the pulses and hence a longer range for fringes. However, in order to scan for a longer duration, the alignment of the setup has to be stable over a long period of time. In order to ensure a good alignment during the whole scan, an automated system for stabilising alignment could be implemented.

In order to increase the total delay range of the setup, another aspect has to be taken in to account. As can be seen in our measurements, the signal of the sideband of interest fades for delays far away from the maximum at around 200 fs. This is partly due to the fact that the delay region of temporal overlap in the MBES is limited by how short the pulses are. By reducing the slit size in the blocking mask, less of the fundamental spectrum is

transmitted through the probe and therefore the probe pulses become longer. The limiting factor here is that by decreasing the slit size, the intensity of the probe is decreased and could potentially affect the signal strength. To increase the resolution and potentially get a better result, the slits size should be optimised.

In Ref. [13] a Bayesian estimation algorithm was used to estimate the parts of the reduced density matrix amplitude that was not measured experimentally. To build on this project, the main diagonal could be measured and then the algorithm could be used to estimate the missing parts of the density matrix.

As discussed earlier, the resolution of the density matrix is limited to the resolution of the recorded photoelectron time-of-flight. By increasing the resolution along the diagonal, a better separation between the spin-orbit splitting could be measured. Also, this would allow for a more detailed reconstruction of the reduced density matrix.

Bibliography

[1] H. Hertz. Ueber einen einfluss des ultravioletten lichtes auf die electrische entladung. *Annalen der Physik*, **267**(8):983–1000, 1887.

[2] A. Einstein. Über einen die erzeugung und verwandlung des lichtes betreffenden heuristischen gesichtspunkt. *Annalen der Physik*, **322**(6):132–148, 1905.

[3] M. Ferray, A. L'Huillier, X. Li, L. Lompre, G. Mainfray, and C. Manus. Multiple-harmonic conversion of 1064 nm radiation in rare gases. *Journal of Physics B: Atomic, Molecular and Optical Physics*, **21**(3):L31, 1988.

[4] P. M. Paul, E. S. Toma, P. Breger, G. Mullot, F. Augé, P. Balcou, H. G. Muller, and P. Agostini. Observation of a train of attosecond pulses from high harmonic generation. *Science*, **292**(5522):1689–1692, 2001.

[5] V. Gruson, L. Barreau, Jiménez-Galan, F. Risoud, J. Caillat, A. Maquet, B. Carré, F. Lepetit, J.-F. Hergott, T. Ruchon, L. Argenti, R. Taïeb, F. Martín, and P. Salières. Attosecond dynamics through a fano resonance: Monitoring the birth of a photoelectron. *Science*, **354**(6313):734–738, 2016.

[6] M. Isinger, R. J. Squibb, D. Busto, S. Zhong, A. Harth, D. Kroon, S. Nandi, C. L. Arnold, M. Miranda, J. M. Dahlström, E. Lindroth, R. Feifel, M. Gisselbrecht, and A. L'Huillier. Photoionization in the time and frequency domain. *Science*, **358**(6365):893–896, 2017.

[7] C. Bourassin-Bouchet, L. Barreau, V. Gruson, J.-F. Hergott, F. Quéré, P. Salières, and T. Ruchon. Quantifying decoherence in attosecond metrology. *Physical Review X*, **10**(3):031048, 2020.

[8] H. Laurell, D. Finkelstein-Shapiro, C. Dittel, C. Guo, R. Demjaha, M. Ammitzböll, R. Weissenbilder, L. Neoričić, S. Luo, M. Gisselbrecht, C. L. Arnold, A. Buchleitner, T. Pullerits, A. L'Huillier, and D. Busto. Continuous-variable quantum state tomography of photoelectrons. *Physical Review Research*, **4**(3):033220, 2022.

[9] P. B. Corkum. Plasma perspective on strong field multiphoton ionization. *Physical Review Letters*, **71**(13):1994, 1993.

[10] H. Laurell. *Attosecond photoelectron interferometry: from wavepackets to density matrices*. PhD thesis, Lund University, 2023.

[11] J. Watrous. *The Theory of Quantum Information*. Cambridge University Press, 2018.

[12] D. Busto, H. Laurell, D. Finkelstein-Shapiro, C. Alexandridi, M. Isinger, S. Nandi, R. J. Squibb, M. Turconi, S. Zhong, C. L. Arnold, R. Feifel, M. Gisselbrecht, P. Salières, T. Pullerits, F. Martín, L. Argenti, and A. L'Huillier. Probing electronic decoherence with high-resolution attosecond photoelectron interferometry. *The European Physical Journal D*, **76**(7):1–10, 2022.

[13] H. Laurell, S. Luo, R. Weissenbilder, M. Ammitzböll, S. Ahmed, H. Söderberg, C. L. M. Petersson, V. Poulain, C. Guo, C. Dittel, D. Finkelstein-Shapiro, R. J. Squibb, R. Feifel, M. Gisselbrecht, C. L. Arnold, A. Buchleitner, E. Lindroth, A. F. Kockum, A. L'Huillier, and D. Busto. Measuring the quantum state of photoelectrons. 2023. (Submitted).

[14] E. J. Pegg. Rulers, arrays, and gracefulness. 2004. http://mathpuzzle.com/MAA/30-Rulers%20and%20Arrays/mathgames_11_15_04.html (Accessed: 2024-05-23).

[15] D. Strickland and G. Mourou. Compression of amplified chirped optical pulses. *Optics communications*, **55**(6):447–449, 1985.

[16] S. Luo, R. Weissenbilder, H. Laurell, M. Ammitzböll, V. Poulain, D. Busto, L. Neoričić, C. Guo, S. Zhong, D. Kroon, R. Squibb, R. Feifel, M. Gisselbrecht, A. L'Huillier, and C. Arnold. Ultra-stable and versatile high-energy resolution setup for attosecond photoelectron spectroscopy. *Advances in Physics: X*, **8**(1):2250105, 2023.

[17] R. Weissenbilder. *Optimization of High-order Harmonic Generation for Attosecond Science*. PhD thesis, Lund University, 2023.

[18] B. Saleh and M. Teich. *Fundamentals of Photonics*. Wiley Series in Pure and Applied Optics. Wiley, 2019.